Direct Dimethyl Ether Synthesis from Syngas on Copper-Zeolite Hybrid Catalysts with a Wide Range of Zeolite Particle Sizes

M. Cai[a], *A. Palčić*[b], *V. Subramanian*[a], *S. Moldovan*[c], *O. Ersen*[c], *V. Valtchev*[b], *V.V. Ordomsky*[a] *and A. Y. Khodakov*[a*]

[a]Unité de catalyse et de chimie du solide (UMR 8181 CNRS), Université Lille 1-ENSCL-EC Lille, Bat. C3, Cité Scientifique, 59655 Villeneuve d'Ascq, France

[b]Laboratoire Catalyse et Spectrochimie, ENSICAEN, 6 Boulevard Maréchal Juin 14050 Caen, France

[c]IPCMS, Université de Strasbourg, 23, rue du Loess BP 43, F-67034 Strasbourg, France

*Corresponding authors: E-mail address: vitaly.ordomsky@univ-lille1.fr (V.V. Ordomsky) andrei.khodakov@univ-lille1.fr (A.Y. Khodakov)

Abstract

This paper reports on the direct dimethyl ether synthesis from syngas on hybrid bifunctional copper-zeolite catalysts. Both laboratory synthetized and commercial zeolites were used in this work. The catalyst performance is evaluated under pressure in a continuous fixed bed milli-reactor. The relationships between zeolite particle sizes, acidity and catalytic performance of the hybrid catalysts in dimethyl synthesis have been studied. The catalysts and catalyst precursors were characterized using a wide range of characterization techniques: nitrogen adsorption-desorption measurements, X-ray diffraction, ^{27}Al NMR, scanning electron microscopy, transmission electron microscopy and Fourier transform infrared spectroscopy with adsorbed molecular probes.

It is found that the reaction rate in direct dimethyl ether synthesis is strongly affected by the sizes of zeolite particles. The hybrid catalysts containing small individual nanosized zeolite particles (60-100 nm) were much active that their counterparts with intergrown crystal agglomerates. The phenomenon is interpreted in terms of enhanced transport of methanol from the copper catalyst to the acid sites in the small zeolite particles with a shift of the thermodynamic equilibrium. The catalyst deactivation was attributed to copper sintering in the presence of the acid sites on the external surface of zeolites. It is established that the catalyst deactivation is less significant with the catalysts containing ZSM-5 zeolites with lower concentration of acid sites on the zeolite external surface. A new methodology to enhance the catalytic performance and stability of copper-zeolite hybrid catalysts for direct dimethyl ether synthesis is proposed.

Keywords: ZSM-5; particle size; dimethyl ether synthesis; external surface acidity; deactivation

1. Introduction

Dimethyl ether (DME) is the simplest ether and is one of the most promising environmentally optimized alternatives [1, 2] to the conventional fossil fuels (gasoline or diesel fuels) due to its high cetane index (> 55), low emission of CO, NO_x, particulates and reduced noise. DME can be used as a substitute for liquefied petroleum gas (LPG) that is widely used as fuel in the industry and household [3].

DME has several interesting characteristics as a fuel. It does not contain either sulphur or nitrogen. It is biodegradable; it has low toxicity and does not corrode metals. In addition, DME is an important intermediate for the production of useful chemicals (i.e. methyl acetate and dimethyl sulphate) and petrochemicals (light olefins, BTX aromatics). DME also provides a new competitive route for production of transportation fuels compared with the LNG technology or Fischer-Tropsch synthesis [4]. The DME produced from biomass (also called bio-DME) is a carbon-neutral fuel from the viewpoint of CO_2 emissions thus contributing to restrain the global warming.

1.1 Dimethyl ether synthesis

In the industry, DME manufacturing usually proceeds in two stages. The relevant reactions are displayed below [5, 6]

$CO_{(g)}+2H_{2(g)}=CH_3OH_{(g)}$ ΔH_0=- 90.4kJ/mol

$2CH_3OH_{(g)}=CH_3OCH_{3(g)}+ H_2O_{(g)}$ ΔH_0=-23 kJ/mol

In the first stage, syngas is converted into methanol. The reaction involves copper based catalysts. The syngas conversion to methanol is limited by the thermodynamics, especially at high temperatures. In the second stage, methanol is dehydrated into DME over acid catalysts.

The two-stage process is currently considered as the most mature route for DME synthesis. Methanol, however, is an expensive chemical feedstock, making the produced DME very costly.

The direct DME synthesis from syngas is an attractive alternative to the two-stage process. The direct DME synthesis, which proceeds on a single catalyst and in a single reactor, overcomes the thermodynamic constraints of methanol synthesis [7, 8, 9] leading to higher per-pass CO conversions and higher DME productivities. Note however that water gas shift reaction which occurs under these conditions, results in significant CO_2 production:

$CO_{(g)}+H_2O_{(g)}=CO_{2\,(g)}+H_{2\,(g)}$ ΔH_0=-41 kJ/mol

1.2 Bifunctional hybrid catalysts for direct DME synthesis

Direct DME synthesis requires highly efficient bifunctional catalytic systems which would combine a carbon monoxide hydrogenation function for methanol synthesis and an acidic function for methanol dehydration. The crucial issue in catalyst design could be therefore, optimization of the catalyst composition and interaction between these catalyst components [10]. Both well-dispersed copper particles with a high reducibility and large amounts of weak acidic sites are required for preparation of the bifunctional catalysts with satisfactory catalytic performance [11]. The hybrid catalysts for direct DME can be prepared using either mechanical mixing of methanol synthesis catalyst and solid-acid catalyst, co-precipitation (sol–gel), impregnation or even more complex methods (e.g. capsule [12, 13], core–shell catalysts [14]). It appears that a strong interaction between hydrogenation and acidic functions in the catalysts prepared by impregnation and co-precipitation could lead to lower activity and poor stability.

The Cu-Zn-Al (CZA) catalyst for methanol synthesis has been successfully developed several decades ago. The advantages of the Cu/Zn systems include low cost and high

selectivity to methanol. The catalyst composition has been carefully optimized in numerous reports [15, 16, 17, 18]. Copper nanoparticles associated with a promoter, i.e. Zn, are usually considered as active phase for methanol synthesis. It is believed that in these nanoparticles copper can be either completely metallic [15] or partially oxidized under the reaction conditions. Other reports [19, 20] suggest, however, that the specific interaction at the Cu/ZnO interface and stabilization of particular Cu morphologies may influence the catalytic performance.

Both carbon monoxide hydrogenation to methanol and methanol dehydration to DME could be kinetically relevant steps in direct DME synthesis. At the temperatures characteristic of direct DME synthesis, carbon monoxide hydrogenation to methanol over copper based catalysts is a reversible catalytic reaction. Recently, major efforts have been dedicated to the design of methanol dehydration active phase in the bifunctional DME synthesis catalysts. The methanol dehydration occurs on an acid catalyst. Alumina has been first used [21, 22, 23, 24] as an acid catalyst for methanol dehydration. The alumina-based catalysts, however, either pure or doped, are relatively sensitive towards deactivation by competitive adsorption of water and also by coke formation. The zeolite based catalysts have several advantages for methanol dehydration to DME in respect to more conventional alumina such as tunable acidity and better stability in the presence of steam [25, 26]. The ZSM-5 zeolite has mostly been used as the acid component in bifunctional DME synthesis catalysts [27]. Other zeolites and microporous materials such as ferrierite [28], MCM-22, ITQ-2, IM-5, and TNU-9, polymeric Naflon resins [29], several microporous silicoaluminophosphates (SAPO-5, -11, -18 and 34) [30] and phosphorus modified γ-Al_2O_3 [31] have also been investigated. The catalytic performance of the zeolites for methanol dehydration was correlated to the concentration of Brönsted acid sites. In addition to zeolite acidity, other zeolite characteristics such as morphology and porous structure could be also important for the design of efficient

catalysts. Composite catalysts for direct DME synthesis from syngas were prepared by Martinez [32] et al. using different zeolites (ZSM-5, FER, IM-5, TNU-9, MCM-22, ITQ-2). The authors attributed difference in the catalyst stability to different zeolite morphology. The ZSM-5 zeolite was found to be more efficient in direct DME synthesis than mordenite [33]. This was attributed to three dimensional pore system of ZSM-5 zeolite which may facilitate diffusion of reagents and reaction products.

The activity of the bifunctional catalysts decreases with time on stream due to the deactivation. The catalysts for direct DME synthesis have been susceptible to deactivation by copper oxidation, sintering [34, 35], coke deposition [36, 37] and contamination with impurities in syngas which could also affect the acid sites of methanol dehydration. Martinez et al [38] attributed the deactivation to the detrimental interactions between the methanol synthesis catalyst and zeolite. The deactivation could be due to the interaction between Al species of zeolite and Cu sites of Cu/ZnO particles at the interface between these two components. Several attempts were made in the literature to improve the stability of these catalysts. Confining of copper nanoparticles within the zeolite matrix was proposed by Garciá-Trenco [38] as an efficient strategy to improve the catalyst stability in direct DME synthesis. It was found that the confined copper catalyst deactivated at a much lower rate than the catalysts prepared by mixing or grinding. Sierra et al [39] attributed long-term catalyst deactivation to coking. Co-feeding with water attenuated coke deposition during the methanol synthesis. It was suggested that water partially inhibited the formation of coke precursors. Our recent report [40] showed that copper sintering, and copper migration leading to the decrease in the concentration of zeolite Brönsted acid sites could be major reasons of deactivation of copper zeolite catalyst prepared by kneading. Zeolite pre-treatment with tetraethyl orthosilicate can slow down [40] the catalyst deactivation and improve the DME productivity.

1.3 Zeolite particle sizes and catalytic performance

Zeolite is an important part of bifunctional catalysts for direct DME synthesis from syngas. The literature shows contradictory information about the effect of particle size on the performance of zeolite catalysts. The influence of zeolite particle sizes on the catalytic performance is often considered in relation with the zeolite shape selectivity [41, 42, 43]. The shape selectivity can be obtained by using the zeolite with channel dimensions approaching the sizes of the reacting molecules. This results in large differences in the diffusivity of linear and non-linear isomers. A significant number of reports [44, 45, 46, 47, 48] have been dedicated to the evaluation of the zeolite particle size and molecular shape selectivity in hydrocracking reactions. No information is available however, about the effect of zeolite particle sizes on the catalytic performance of copper-zeolite catalysts in DME synthesis.

It is still not clear whether large or small zeolite particles could be optimal for this reaction. Jentoft et al [46] found that the activity, selectivity and stability of the K-LTL zeolite-supported platinum catalysts in n-hexane reforming could be correlated with the ratio of the external surface area to the intracrystalline pore volume. Bonetto et al [47] tested the beta zeolite with different crystal sizes in gas-oil cracking. The zeolite with the optimum crystallite size of 0.40 μm showed the best performance in terms of stability, activity and selectivity. The beta zeolite with a wide range of particle sizes was also tested as catalyst for degradation of high density polyethylene [48]. Zeolite nanoparticles with very large external surface area showed the best performance in this reaction. In the conversion of methyl cyclohexane, the USY zeolites with the crystallite sizes in the range between 0.4 and 0.9 μm mostly affected the product distribution rather than the conversion. The selectivity variations were associated with hydrogen transfer, ring-opening/cracking and transalkylation

The effect of zeolite crystallite sizes was also studied for methanol conversion reaction. Smaller H-UZM-12 zeolites [49] were found less active and stable in this reaction,

probably because of fast build-up of bulky coke molecules on the external surface of zeolite crystallites. Coke deposition inhibited the methanol diffusion to intrazeolitic acid sites, rendering them ultimately inaccessible for catalysis. The SAPO-34 and ZSM-5 crystallites of 200–500 nm showed [50] the best conversions and lifetimes because of their large external surfaces and short diffusion lengths. The zeolites with the smallest crystallites (<150 nm) deactivated more rapidly due to pore blocking by heavy coke deposits. Note however, that the effect of zeolite crystallite sizes could be even more complex for bifunctional catalysts, where in addition to chemical reaction, the transport of reagents and intermediates between different active phases should be taken into consideration. Very often in addition to individual crystallites, zeolites also contain agglomerates. In the composite catalysts prepared by mechanical mixing the presence of these agglomerates may significantly affect transport of reacting molecules and thus, having strong influence on the catalytic performance.

The goal of the present work is to elucidate the influence of zeolite particle sizes and acidity on the performance and stability of the copper-zeolite hybrid bifunctional catalysts for direct DME synthesis from syngas and to suggest a new methodology for the improvements of the catalyst activity, selectivity and stability. A series of hybrid catalysts were prepared using ZSM-5 zeolites with different crystallite or aggregate sizes. The catalysts and catalyst precursors were characterized using a combination of characterization techniques: nitrogen adsorption-desorption measurements, X-ray diffraction (XRD), ^{27}Al NMR, scanning electron microscopy (SEM), transmission electron microscopy (TEM-HAADF) and Fourier transform infrared spectroscopy (FTIR) with adsorbed molecular probes. The catalyst performance in direct DME synthesis was investigated in a fixed bed reactor. The experiments were conducted beyond 100 h in order to evaluate the influence of the catalyst structure on the deactivation rate under the reaction conditions.

2. Experimental

2.1. Zeolite synthesis

The chemicals used to prepare the nano-sized ZSM-5 crystallites were sodium aluminate (Riedel de Haën, w(Al_2O_3) = 54%, w(Na_2O) = 41%), tetra-n-propylammonium hydroxide (TPAOH, Alfa Aesar, 20 wt.% water solution), tetraethyl orthosilicate (TEOS, Aldrich, 98%) and distilled water produced in our laboratory. Appropriate amounts of sodium aluminate, TPAOH and water were mixed and stirred with magnetic stirrer until the system gets clear. Thereafter, TEOS was added to the solution and hydrolyzed at 80 °C for 24 h. The final molar oxide composition of the reaction mixture was $1.23Na_2O$:9.74 TPAOH:$1.0Al_2O_3$:$43.2SiO_2$:$806H_2O$. Aliquots of clear solution were divided in four autoclaves and heated at 100, 120, 150 and 170 °C. The synthesis duration at 120, 150 and 170 °C was 5 days. The synthesis at 100°C was performed for 7 days. Recovered solid phases of the samples were washed with distilled water until the pH of the supernatant was 7, dried at 80 °C and calcined at 550 °C for 5 h (heating rate 1.75 °C/min). The protonic zeolite forms were obtained by calcining the NH_4^+ form of zeolite at 550°C for 5 h with the ramp of 2 °C/min in a flow of synthetic air (40 cm^3/min).

The ZSM-5 samples are labelled according to average particle size which was calculated from the SEM images. The average zeolite particle size was determined by the measuring the size of 30 particles for the nanosized ZSM-5@65-110 samples, and 20 particles for the ZSM-5@500-800 samples. The histograms of zeolite particle size distribution are displayed in Figure S1, Supporting Material (SM). The Sauter average zeolite particle size calculated from the histograms is given in Table 1. The individual zeolite size of the laboratory synthetized samples increases with the crystallization temperature: ZSM-5@65 (100°C), ZSM-5@80 (120°C), ZSM-5@95 (150°C) and ZSM-5@110 (170°C). Commercial ZSM-5 zeolites with larger crystallite agglomerates (500 nm and 800 nm) were also used in

this work. The ZSM-5@500 sample with Si/Al ratio of 45 was provided by Süd-Chemie. ZSM-5@800 with Si/Al ratio of 25 was purchased from Zeolyst.

2.2. Preparation of CZA catalyst

The $CuO–ZnO–Al_2O_3$ precursor (Cu:Zn:Al = 60:30:10 atomic ratio) was prepared by co-precipitation using a solution containing metal nitrates ($[Cu^{2+}]+[Zn^{2+}]+[Al^{3+}]$ =1.0 M) and a sodium carbonate solution at constant pH (ca. 7) and constant temperature (70 ˚C). The suspension was continuously stirred and kept at the desired pH by adjustment of the relative flow rates of the two solutions. The final suspension was aged under stirring at 70 ˚C for 1 h. The precipitate was filtered off, repeatedly washed with sufficient amounts of deionized water to remove residual sodium ions, dried at 110 ˚C overnight and then finally calcined at 350 ˚C in flowing air for 6 h yielding the oxide $CuO–ZnO–Al_2O_3$ (CZA) catalyst.

The hybrid catalysts were prepared by physically mixing the powders (under 150 mesh) of the prepared CZA catalyst and zeolite (5:3 wt/wt), pressing the mixture into tablets and finally crushing them into granules before the reaction.

2.3. Characterization

The chemical composition of the synthetized zeolites was determined by inductively coupled plasma–atomic emission spectrometer (ICP-AES) OPTIMA 4300 DV (Perkin–Elmer). The BET surface area, pore volume and average pore diameter were determined by N_2 physisorption using a Micromeritics ASAP 2000 automated system. The BET surface area and pore size distribution in mesoporous silicas were measured using N_2 adsorption-desorption at -196°C. Each sample was degassed under vacuum at <10 μmHg at 300 °C for 4 h prior to N_2 physisorption. The total pore volume (TPV) was calculated from the amount of vapor adsorbed at a relative pressure close to unity assuming that the pores are filled with the

condensate in liquid state. The pore size distribution curves were calculated from the desorption branches of the isotherms using Barrett–Joyner–Halenda (BJH) formula [51]. The catalyst external surface area and micropore volume were calculated using deBoer t-plot method [52].

The prepared samples were analyzed by X-ray diffraction using PANalytical X'pert PRO MPD diffractometer with Cu-Kα monochromatized radiation (λ = 1.5418 Å, 45 kV, 40 mA). The measurements were performed in the range of Bragg's angles 2θ = 5-50°, step size of 0.0167°, time per step of 99.68 s.

The TEM analysis were carried out on a Jeol 2100F (field emission gun) microscope operating at 200 kV equipped with a probe corrector for the spherical aberrations. The point-to-point resolution reached was on the order of 2 Å under the parallel TEM mode and 1 Å under the STEM mode. For a better chemical resolution, the micrographs were also acquired in the HAADF mode by using a spot size of 1.1 Å with a current density of 0.5 $pA*Å^{-1}$.The energy X-ray dispersive spectroscopic analyses have been performed by using a Li-Si EDS detector with an energy resolution of 0.03 eV. Prior to the analysis, the sample was dispersed by ultrasound in ethanol solution for 5 min, and a drop of solution was deposited onto a carbon membrane onto a 300 mesh-copper grid.

The infrared spectra were recorded with a Nicolet Magna 550-FT-IR spectrometer at 4 cm^{-1} optical resolution. Prior to the measurements, each sample was pressed into self-supporting disc (diameter: 2 cm, 13 mg) and pretreated in the IR cell attached to a vacuum line at 120°C (0.33 °C/min) for 1.5 h first and then at 500 °C (1.27 °C/min) for 2 h under the pressure of 10^{-6} torr. The adsorption of pyridine and lutidine (2,6-dimethylpyridine) was performed at 150 °C. After establishing a pressure of 1 Torr at equilibrium, the cell was evacuated at room temperature. In order to study the strength of the interactions between the zeolite and the probe molecules, the samples were heated to 50-400 °C (step 50 °C) and the

spectra were taken at each temperature. Then, the amount of Brönsted acid sites at each desorption temperature was calculated from the integrated area of the bands (after background subtraction) of adsorbed pyridine at ca. 1545 cm^{-1} and 1490 cm^{-1} or from the bands of adsorbed lutidine at 1610 and 1640 cm^{-1} using the extinction coefficients reported by Emeis [53] and Onfroy [54].

The electron micrographs were obtained by MIRA-LMH (Tescan) scanning electron microscope (SEM) equipped with field emission gun. ^{27}Al MAS NMR spectra were recorded on a Bruker Avance III (11.7 T) spectrometer using 4 mm-OD zirconia rotors and a spinning frequency of 14 kHz. Pulse recycling delay was 1 s and a pulse length of 2.5 microseconds ($\pi/12$, selective pulse was applied). The chemical shifts were referred to a 0.1 M aqueous solution of 0.1 M $Al(NO_3)_3$. The acquired spectra were normalized with respect to the mass of the corresponding sample.

2.4. Catalytic tests

The DME synthesis reaction was carried out in a fixed-bed stainless-steel tubular reactor (d_{int} =8 mm) operating at high pressure. The catalyst loading was typically 0.5 g. Before reaction, the samples were reduced in hydrogen flow with the flow rate of 30 cm^3/min. During the reduction, the temperature was increased to 290 ˚C with a heating rate of 2˚C/min and then kept at this temperature for 7 h. After reduction, the hydrogen flow was switched to syngas mixture with H_2/CO molar ratio of 2. The reaction was carried out at 260 ˚C under a pressure of 20 bar maintained using a back pressure regulator, and the gas hourly space velocity (GHSV) of 3600 cm^3/g/h. The tests were conducted continuously for at least 100 h in order to evaluate the deactivation behavior of the cataysts. Carbon monoxide contained 5% nitrogen, which was used as an internal standard for conversion and selectivity calculations. The products were sampled from the high pressure side and analyzed using an online gas

chromatograph with TCD (N_2, CO, CO_2 and CH_4) and FID (MeOH, DME and hydrocarbons) detectors.

3. Results

3.1. Zeolite morphology and texture

The XRD patterns of the ZSM-5 samples are shown in Figure 1. The patterns are almost identical, as all the diffraction peaks obtained can be indexed to MFI-type structure [55]. The high peak intensities and absence of the baseline drift in diffraction patterns of both as-synthesized and commercial ZSM-5 zeolites indicate good crystallinity.

Scanning electron microscopy (SEM) is an efficient tool for investigation of zeolite morphology. Representative SEM micrographs of zeolite samples are displayed in Figure 2. The zeolites synthetized in this work (ZSM-5@65, ZSM-5@80, ZSM-5@95 and ZSM-5@110) exhibit crystallites in the nano-scale range with size below 200 nm. The crystallite size increases as the crystallization temperature increases from 100 to 170°C, whereas single crystallites dominate the product synthesized at 150°C and 170°C. According to the SEM study the solids obtained at 100°C and 120°C are intergrown agglomerates. Differently to the samples synthetized in this work, the commercial ZSM-5@500 and ZSM-5@800 contain larger crystallite aggregates which involve a larger number of individual zeolite nanocrystals. The average sizes of zeolite particles determined by SEM are given in Table 1. The average particle size of ZSM-5 samples varies from 63 nm in ZSM-5@65 sample to 810 nm in ZSM-5@800.

The isotherms of nitrogen adsorption-desorption on the zeolites are shown in Figure 3a. The BET surface area of the zeolites varies between 305 and 400 m^2/g. As expected, the external surface area also varies with the sizes of the zeolite individual crystallites. The isotherms of all the zeolites exhibit an uptake at low partial pressure indicative of the presence

of micropores. The ZSM-5@800 sample displayed a Type-I isotherm, fast uptake at low relative pressure is followed by plateau without hysteresis, which is usually observed for microporous materials with relatively low external surface areas [15]. Other zeolites exhibit a combination of Type I and IV isotherms which besides the uptake at low relative pressure exhibit a hysteresis loop at high relatively pressure ($P/P_o > 0.8$). The presence of hysteresis at high relative pressures indicates the presence of larger meso- and macropores. The H1 type hysteresis is usually attributed to filling and emptying of cylinder mesopores of rather constant cross section [56]. The BJH mesopore size distribution curves are shown in Figure 3b. The evaluation of average mesopore sizes using BJH method gives the values between 25 and 50 nm in the zeolite samples. It is worth mentioning that the mesopore diameter increases with the increase in the zeolite crystallite sizes from ZSM-5@60 to ZSM-5@110.

^{27}Al MAS solid state NMR spectra (Figure 4) were collected for selected samples in order to determine the effect of particle size on the environment around the aluminum atoms in the framework. The spectra display a strong peak with chemical shift of 50 ppm, which corresponds to tetrahedrally coordinated framework aluminum [57]. Additionally, a weak peak was observed at 0 ppm indicating the presence of a small amount of extra framework octahedrally coordinated aluminum in the samples. The intensity of the signal at 50 ppm is weaker on ZSM-5@65 and ZSM-5@80, indicating their lower framework Al content. Closer inspection of the corresponding ^{27}Al NMR spectra reveals also the presence of a peak at 29 ppm that could be attributed either to perturbed tetrahedrally coordinated or penta-coordinated aluminum in these two samples. Therefore ^{27}Al NMR results indicate, however, lower amount of tetrahedral Al in very small zeolite nanoparticles (Table 1 in Supporting Material) in ZSM-5@65 and ZSM-5@80 zeolites. This suggests lower concentration of Brönsted acid sites in smaller nanoparticles compared to the samples with large ones. Further remark is the observation that the total intensity of the signals in the spectrum of sample

ZSM-5@95 is stronger than the other samples. The possible reason for this is the fact that despite of high crystallinity the presence of amorphous phase in quantities below XRD detection limit as well as highly distorted Al species which are thus "NMR invisible" in the samples cannot be excluded. Only tetrahedrally coordinated Al^{3+} ions are found in the commercial samples.

3.2. Zeolite acidity

To study the influence of morphology on the concentration and acidic properties of ZSM-5 hydroxyl groups, we have investigated their FTIR spectra. The FTIR spectra exhibit an intense peak at 3740 cm^{-1}, which can be attributed to silanol hydroxyl groups on the external zeolite surface or silanol groups related to the defect sites [58]. A peak at 3620 cm^{-1} is also observed which can assigned to the bridged Si-OH-Al groups which correspond to the zeolite Brönsted acid sites [59]. The intensity of the FTIR band at 3620 cm^{-1} assigned to the bridged hydroxyl groups increases with the increase in zeolite crystallite sizes from ZSM-5@65 to ZSM-5@110.

The band at 3740 cm^{-1} can be decomposed into three bands, i.e., 3745 cm^{-1}, 3735 cm^{-1} and 3726 cm^{-1}, which are assigned to external, intracrystalline and silanols in zeolite channels, respectively [60, 61]. The shape of this band, which differs in studied samples, is a function of the contribution of each of these silanols. ZSM-5@65 and ZSM-5@80 have larger external surface area due to very small crystallites and respectively the band at 3745 cm^{-1} is more intense. Less intense and broader band was observed in the samples with lower external surface area, namely ZSM-5@95 and ZSM-5@110. The peaks related to internal silanol groups clearly indicate the presence of defect sites in the zeolite framework. The highest amount of internal silanols was observed in ZSM-5@65 and ZSM-5@80 samples, which are synthesized at relatively low crystallization temperature. The results are consistent with the N_2

adsorption and ^{27}Al MAS NMR data which revealed somewhat lower crystallinity of these samples. It should be noted that the home made nano ZSM-5 samples exhibit a peak at about 3670 cm^{-1}. These peaks might be associated with extra framework aluminum species, which is in good agreement with the ^{27}Al MAS NMR study [62].

The FTIR spectra of adsorbed pyridine (Py, pK_b=3.5) were used for characterization of both Brönsted and Lewis acidic sites in the zeolites [63]. The IR spectra of the zeolites with pyridine adsorbed at 150 °C are shown in Figure 6. The intense IR bands at 1540, 1490 and 1450 cm^{-1} are observed. The bands at 1540 cm^{-1} is attributed to Py adsorbed on Brönsted acid hydroxyl group of the zeolites (PyH^+ species), while the band at 1450 cm^{-1} corresponds to Py adsorption on the zeolite Lewis acid sites. The results obtained using pyridine adsorption is consistent with the characterization of hydroxyl groups in the zeolites using FTIR spectroscopy (Figure 5). The peak at 1490 cm^{-1} is due to pyridine adsorbed on both Brönsted and Lewis acid sites. It can be observed that the intensity of these three bands corresponding to Brönsted and Lewis acid sites decreases in the order: ZSM-5@800>ZSM-5@500 > ZSM-5@110 ≈ ZSM-5@95> ZSM-5@80 > ZSM-5@65. The amounts of Py adsorbed on Brönsted (BS) and Lewis acid sites (LS) in the zeolites calculated from the FTIR data are shown in Table 1. The spectra of adsorbed pyridine indicate higher concentration of both Brönsted and Lewis acid sites in the zeolite samples containing larger crystallite agglomerates. Indeed, the intensity of IR bands at 1540 and 1450 cm^{-1} are significantly higher in ZSM-5@800 zeolite compared to ZSM-5@80. Note that both samples have the same Si/Al ratio. Hence, one might suggest that smallest nanoparticles contain less Brønsted and Lewis acid sites than larger ones that might be related with specific conditions of the synthesis of the nanosized crystals.

In general, the Lewis acid sites are related with the presence of extra framework metal species. Therefore an analysis of ^{27}Al MAS NMR spectra was performed. The deconvolution of the spectra allowed evaluating the fraction tetra-, penta- and octahedrally coordinated

aluminum (Table S1). No correlation between the number of extra framework aluminum and the number of Lewis acid sites was found. Hence, one may conclude that not all extra framework aluminum species act as Lewis acid sites. It should also be noted that the two industrial samples exhibit solely a tetrahedral aluminum, yet they poses a notable amount of Lewis acid sites. Although special precautions were taken the presence of "NMR invisible" aluminum cannot be excluded, which make difficult the correlation between solid state NMR and IR data.

3.3. Acidity of the external surface of zeolite crystallites

The zeolite acidity on the external surface of zeolites was characterized by lutidine (2,6-dimethylpyridine, pK_b=8.7) adsorption. The diameter of lutidine (6.7 Å) is larger than the channel diameter of ZSM-5 zeolites. This molecule is often used for evaluation of the acid sites located on the external surface and in the meso- and macropores of zeolites [64]. The FTIR spectra of adsorbed lutidine are shown in Figure 7. The spectra show the FTIR bands at 1610 and 1640 cm^{-1} which can be assigned to the lutidine molecules adsorbed on the Brönsted sites located on the outer surface of the zeolites. The amounts of adsorbed lutidine were calculated using the extinction molar coefficients of protonated lutidine [54]. The amounts of adsorbed lutidine are shown in Table 1. The concentration of protonated lutidine is also different for the zeolite with different crystallite sizes, followed by the order: ZSM-5@800>ZSM-5@500 >> ZSM-5@95 ≈ ZSM-5@110≈ ZSM-5@80 ≈ ZSM-5@65.

3.4 Characterization of the CZA methanol synthesis catalyst

The CZA catalyst was prepared using conventional coprecipitation. The XRD patterns of the calcined CZA catalyst are presented in Figure S2 (SM). They are consistent with previous reports [65, 66, 67]. Only CuO and ZnO diffraction peaks are detected. No

diffraction peaks of Al_2O_3 phase were present even at aluminum content of 10%. This suggests that aluminum oxide is probably present in the amorphous form. The XRD peaks at 32.5°; 35.5°; 38.7°; 48.7°; 58.3°; 61.5°; 67.9° were assigned to the CuO tenorite phase, while the peaks in 2θ = 31.8°; 36.3°; 47.7°; 62.9° were attributed to the ZnO zincite phase. After the reduction the copper particles in CZA catalysts were measured by TEM. The copper nanoparticles with mean size of 5 nm or embedding the plate like Zn and Al oxide grains were detected. The thickness of the Cu metallic layer varies from a few to 15 nm (Figure S3, SM).

The H_2-TPR profile (Figure S4, SM) of the CZA catalyst exhibits a broad reduction peak at 270 °C. The peak integration suggests that in the temperature range from room temperature to 400 °C, hydrogen consumption corresponds to the reduction of CuO into metallic copper. The TPR profiles of the CZA are also consistent with previous reports [65].

3.5. Catalytic performance in direct DME synthesis

The catalytic performance data of mechanical mixtures of CZA and zeolite with different crystallite sizes at 260°C and 20 bar are given in Figure 8 and Table 2. Dimethyl ether, methanol, carbon dioxide, hydrocarbons and water were the major products of carbon monoxide hydrogenation. Figure 8 displays CO conversion measured on different catalysts at GHSV=3600 $cm^3/g_{cat}\cdot h$ as a function of reaction time. Carbon monoxide conversion slowly decreases with time on stream which can be attributed to the catalyst deactivation. Previous reports [40] suggest that the deactivation of CZA/ZSM-5 catalysts can be due to several phenomena: copper sintering, copper oxidation and migration to the cationic positions of zeolite, coke deposition.

Interestingly, carbon monoxide conversion rate is principally affected by the zeolite particle sizes. Higher reaction rate is observed on the catalysts containing smaller individual zeolite crystallites, while the reaction rate was much lower on the catalysts containing larger

zeolite crystallite agglomerates (CZA-ZSM-5@500, CZA-ZSM-5@800). At GHSV=3600 cm^3/g_{cat} h (Table 2), the CO conversion showed the following order of activity for the hybrid catalysts: CZA-ZSM-5@95 > CZA-ZSM-5@110 > CZA-ZSM-5@80 > CZA-ZSM-5@65 > CZA-ZSM-5@500 > CZA-ZSM-5@800. The CO conversion profiles over the CZA-ZSM-5 hybrid catalysts widely varied with the particle size of ZSM-5: nano-sized ZSM-5@95, ZSM-5@110, and ZSM-5@80 maintained CO conversion of 83.2%, while the ZSM-5@500 and ZSM-5@800 zeolites exhibited lower CO conversion. The catalytic results obtained at carbon monoxide conversion between 60 and 80% indicate much slower deactivation of the hybrid catalysts constituted by smaller individual zeolite crystallites. The following order relative to the deactivation rate was observed for the studied catalysts: CZA-ZSM-5@800 > CZA-ZSM-5@500 > CZA-ZSM-5@65 > CZA-ZSM-5@80 > CZA-ZSM-5@110 > CZA-ZSM-5@95.

To evaluate in a more comprehensive manner the influence of the carbon monoxide conversion on the reaction selectivity, the catalytic tests with the hybrid CZA/ZSM-5 catalysts were conducted at different gas spaces velocities. The results are shown in Table 2. As expected, higher gas space velocity leads to lower carbon monoxide conversion which was accompanied by noticeable modifications in the selectivity patterns. DME synthesis is a consecutive reaction which involves carbon monoxide hydrogenation to methanol followed by methanol dehydration. The selectivity of carbon monoxide hydrogenation could be dependent on the conversion level. Methanol is a primary product of carbon monoxide hydrogenation. As expected, the selectivity to methanol is higher at lower carbon monoxide conversion. At higher conversions, however, only very small amounts of methanol are produced. Note that even at the same conversion level, higher methanol selectivity (at the expense of DME selectivity) was observed on the catalysts with larger zeolite agglomerates (CZA-ZSM-5@500 and CZA-ZSM-5@800). Carbon dioxide selectivity however is not influenced by carbon monoxide conversion. Higher selectivity to carbon dioxide at different

conversions can be due to very high rate of water gas shift reaction under the reaction conditions. Carbon dioxide formation is also favored by thermodynamics. Hydrocarbons are only present in trace amounts; their selectivity is not much affected by carbon monoxide conversion.

4. Discussion

4.1. Zeolite particle sizes and performance of bifunctional hybrid CZA-ZSM-5 catalysts for DME synthesis

The present work reveals a strong impact of zeolite particle size on the catalytic performance of CZA-ZSM-5 catalyst in direct DME synthesis from syngas. DME synthesis involves bifunctional catalysts. Carbon monoxide hydrogenation to methanol occurs on copper catalysts, while methanol dehydration involves the ZSM-5 zeolite. Methanol synthesis over the copper catalysts at 260 °C is a reversible reaction. At the reaction temperatures employed in this work, the yield of methanol from H_2/CO over a methanol synthesis catalyst would be principally dependent on the thermodynamic equilibrium rather than on the reaction kinetics. Addition of methanol dehydration function to the methanol synthesis catalysts shifts the thermodynamic equilibrium and favors DME formation. Methanol dehydration involves the zeolite acid sites [68]. In binfunctional copper zeolite catalysts the DME yield could be a function of the rates of both methanol synthesis and methanol dehydration. The concentration and distribution of zeolite acid sites is therefore important for DME productivity.

The results obtained in the present work show that in addition to the zeolite acidity, the zeolite crystallite size and crystallite aggregation can also strongly affect the rate of direct DME synthesis. The rate of carbon monoxide conversion versus reciprocal zeolite particle sizes is shown in Figure 9. Higher DME production rates were observed on the catalysts containing smaller zeolite crystallites, while the reaction rate was much lower in the catalysts

with larger zeolite aggregates. Surprisingly, that zeolite size has even a more significant effect of the reaction rate than the concentration of Brönsted acid sites. Indeed, the overall concentration of Brönsted acid sites measured by Py adsorption was higher in ZSM-5@500 and ZSM-5@800 than in the ZSM-5@65, ZSM-5@80, ZSM-5@95 and ZSM-5@110 which contain smaller particles. ZSM-5@500 and ZSM-5@800 are built up of smaller but heavily intergrown crystallites. This limits the access to crystallite surface. Despite of lower concentration of zeolite acid sites, much higher carbon monoxide DME production rate was observed on the catalysts containing smaller highly accessible zeolite particles.

The concept of multi-functional catalysis was developed by Weiss [69]. It was suggested that in bi-functional catalysis, the kinetic steps of the consequent reactions are coupled to each other through the processes of diffusion of these intermediates from one type of sites to another. The two types of active sites in bifunctional catalysts should be as closer as possible for higher catalytic activity and selectivity [70]. Depending on the diffusion rate of the reaction intermediates, the observed influence of the zeolite particle size on the rate of DME synthesis can be due to at least two different phenomena. First, it can be assumed that in bifunctional CZA-ZSM-5 catalysts methanol dehydration preferentially occurs on the zeolite external surface or in the mesopores. Because of diffusion limitations under the reaction conditions, the acid sites located inside the zeolite crystallite would be less accessible for the reacting molecules. However, our recent work [40] has ruled out this hypothesis. In this work the zeolite external surface was silylated with TEOS in order to reduce its acidity. The catalytic data obtained with silylated zeolites did not shown any significant decrease in the reaction rate. It seems that the dehydration proceeds with similar rate over the acid sites located on the outer surface and in the pore of the zeolites. This suggests that the acidity of zeolite external surface or mesopores is not a determining factor for higher carbon monoxide hydrogenation rate.

The second hypothesis which can explain the positive effect of smaller zeolite crystallites on the catalytic performance can be assigned to the enhanced transport of methanol produced on the CZA catalyst to the ZSM-5 crystallites for dehydration. In this case, smaller zeolite particles (crystallites or agglomerates) reduce methanol transport limitations and diffusion path inside the zeolites. The dehydration in this case occurs both inside the zeolite crystallite and on the external surface. The reaction rate is probably strongly affected by the methanol transport from the methanol synthesis catalyst to the zeolite external surface which serves as an interface between hydrogenation and acidic component in the bi-functional catalysts. The rate of methanol transfer depends on the interface between CZA and ZSM-5 phases which could be much larger for smaller zeolite particles. Smaller crystallite sizes or mesopores lead to shortening the diffusion path lengths and improve transport of the reaction intermediates [71]. The presence of larger zeolite agglomerates in ZSM-5@500 and ZSM-5@800 makes the contact between the methanol synthesis catalyst and zeolite more difficult. Figures 10 and 11 show STEM-HAADF micrographs of the CZA-ZSM-5@500 catalysts prior and after reaction, respectively. It can be seen that the contact between CZA and ZSM-5 components is strongly affected by the size and roughness of the zeolite particles. The zeolite grain size ranges from tens of nm up to few hundred of nm. A poor contact between methanol synthesis catalysts and zeolite agglomerates in the catalyst prepared by mechanical mixing leads to significant transport limitations for methanol and thus to lower overall reaction rate.

The influence of transport phenomena on the reaction rate and selectivity was previously observed for hydroisomerisation reactions occurring on Pt/zeolite catalysts. Guisnet et al. [72] showed that the rate and selectivity of n-C_{16} hydroisomerization is determined by the degree of intimacy between metallic and acidic functions. Recently Kim et al. [73] investigated the effect of zeolite crystal thickness and Pt location on the performance

of bi-functional Pt/ZSM-5 catalysts for hydroisomerisation and observed similar phenomena. The hypothesis about enhanced transport of the reaction intermediates in the catalysts containing smaller zeolite crystallites is also consistent with the selectivity data measured for the catalysts containing zeolite with variable crystallite sizes. Higher methanol selectivity systematically was observed on CZA-ZSM5@500 and CZA-ZSM-5@800 at different conversion levels. This indicates much slower methanol dehydration on the catalysts containing larger zeolite particles which probably arises due to the mass transfer limitations. Our results suggest that in addition to the size for individual zeolite crystallites, the presence of zeolite agglomerates may also significantly affect the rate of catalysts reactions in bifunctional catalysts. Indeed, the rate of diffusion seems to be limited not by individual zeolite crystallite sizes but by the diameter of zeolite intergrown agglomerates.

4.2. Catalyst stability

The bifunctional CZA-ZSM-5 catalysts for direct DME synthesis prepared using zeolites with a wide range of crystallite sizes showed different stability. Nano-sized ZSM-5@95, ZSM-5@110, and ZSM-5@80 did not show appreciable deactivation for up to 100 h, while the ZSM-5@800 and ZSM-5@500 zeolites are noticeably deactivated. The fact that the deactivation took place on a sample containing small crystallites (ZSM-5@500), which are heavily agglomerated and thus built larger particles, show that the accessibility to zeolite crystals is of paramount importance. Catalyst deactivation was more significant at higher carbon monoxide conversion (60-80%). First, we evaluated the role of total zeolite Brönsted acidity in the catalyst deactivation. No reasonable correlation between the deactivation rate and total concentration of Brönsted acid sites measured using Py adsorption was observed.

The deactivation CZA-ZSM-5 catalysts can be due to several phenomena: copper sintering [35] copper oxidation, carbon deposition… Copper sintering was observed in this

work by TEM. From the electron microscopy micrographs, Cu-based nanoparticles deposited on the support under two configurations were observed: nanoparticles with sizes from 1 to 7 nm (see the histogram in Figure 10 accounting for the size of 150 nanoparticles) onto ZSM-5 and those homogenously covering the Zn oxide and alumina grains by following the grains geometry (light contrast in the STEM-HAADF micrographs). After reaction, the particles size increases significantly to values comprised between 7 and 25 nm and a mean value centered at about 15 nm. The detailed mechanisms of deactivation of hybrid copper-zeolite catalysts have been further disclosed in previous reports. Those reports emphasize the role of external zeolite surface in catalyst deactivation. Garcia-Trenco et al [74] attributed deactivation of hydride CZA-ZSM-5 catalyst to the aluminum extra framework species located at the surface of contact between the CZA and zeolite particles. It was suggested that these species could migrate to the CZA catalyst during DME synthesis through a water-assisted mechanism, modifying the interaction between Cu and ZnO_x. On the basis of ex-situ characterization conducted in our recent report [40], deactivation of CZA-ZSM-5 catalyst was attributed to copper sintering, oxidation and ion exchange, which are enhanced in the presence of higher concentration of Brönsted acid sites on the external surface of zeolite. Indeed, Figures 10 and 11 show significant increase in copper particle size during the reaction from few nm up to few tens of nm. The deactivation was slowed down by neutralization of the acid sites on the zeolite outer surface with tetraethyl orthosilicate.

In order to further clarify the effects of the external surface acidity on the deactivation of hybrid catalysts with variable zeolite crystallites, the deactivation rates of different catalysts were compared as a function of the concentration of Brönsted acid sites on external zeolite surface area. The surface sites on the external surface of zeolite were measured by lutidine adsorption. Figure 12 shows the catalyst deactivation rate measured at carbon monoxide conversion of 50-80% versus the concentration of Brönsted acid sites on the

external surface of zeolites estimated from the lutidine adsorption. A more rapid deactivation occurs on the catalysts with higher concentration of acid sites on the external surface. Very high concentration of Brönsted sites on the external surface of ZSM-5@800 (Table 1) leads to a higher deactivation rate. At the same time, ZSM-5@95 which has a lowest surface acidity on the external surface showed better stability. In agreement with previous report [40], higher surface acid sites of zeolite could lead to intensification of the Cu migration, which results in copper sintering during DME synthesis. A decrease in the number of acid sites on the zeolite external surface can lead therefore to better catalyst stability.

5. Conclusion

The obtained results point out a correlation between the performance of bifunctional hybrid CZA-ZSM-5 catalysts for direct DME synthesis and zeolite particle sizes. The catalyst containing smaller individual zeolite crystallites showed higher carbon monoxide conversion rates and higher DME productivities. The observed effects were attributed to the methanol transport phenomena in bifinctional hybrid catalysts from the copper catalyst to the zeolite acid sites. The methanol transport is enhanced in the catalysts containing smaller zeolite crystallites, while the presence of crystallite intergrown agglomerates introduces diffusion limitations. The influence of zeolite particle sizes on the catalytic performance seems even more significant than the effect of total concentration of zeolite Brönsted acid sites.

The catalysts showed noticeable deactivation with time on stream. The deactivation rate was correlated with the concentration of Brönsted acid sites on the external surface of zeolite crystallites. Lower concentration of Brönsted sites on the zeolite external surface leads to a less rapid deactivation and better stability of copper-zeolite hybrid catalysts.

The results obtained in this manuscript indicate a new methodology for catalyst design for direct DME synthesis from syngas. Smaller zeolite ZSM-5 crystallite size and lower

concentration of Brönsted acid sites on the zeolite external surface seem to be beneficial for the design of active, selective and stable hybrid CZA-ZSM-5 catalysts for direct DME synthesis from syngas.

6. Acknowledgments

This research was performed within the ANR project CATSYN-BIOFUELS (ANR-12-BS07-0029-02). The authors gratefully acknowledge the support of the French National Research Agency. M.C. thanks the China Scholarship Council for the PhD fellowship to support her stay at UCCS of France. A.P. acknowledges the Region of Lower Normandy for financial support.

Figure Captions

Figure 1. XRD patterns of ZSM-5 zeolites. The patterns are offset for clarity

Figure 2. Representative SEM images of the series of ZSM-5 samples.

Figure 3. Nitrogen adsorption-desorption isotherms (a) and BJH mesopore size distribution curves. The nitrogen adsorption-desorption isotherms are offset for clarity.

Figure 4. Normalized ^{27}Al MAS NMR spectra of the series of ZSM-5 samples. The spectra are offset for clarity.

Figure 5. FTIR spectra of zeolite in the region of OH stretching vibrations. The spectra are offset for clarity.

Figure 6. FTIR spectra of zeolites with adsorbed pyridine. The spectra are offset for clarity.

Figure 7. FTIR spectra of zeolites with adsorbed lutidine. The spectra are offset for clarity.

Figure 8. Carbon monoxide conversion on the hybrid CZA-ZSM-5 catalysts as function of time on stream (T=260°C, P=20 bar, H_2/CO=2, GHSV=3600 cm^3 /g_{cat} h)

Figure 9. Reaction rate as a function of reciprocal zeolite crystallite size in hybrid CZA-ZSM-5 catalysts.

Figure 10. Localization of copper methanol synthesis component within the fresh CZA-ZSM-5@500 containing larger intergrown zeolite agglomerates by STEM-HAADF analysis. Cu-based nanoparticles with sizes between 2 and 7 nm are disposed on the ZSM-5 grains or on the surface of the ZnO and alumina grains.

Figure 11. Localization of copper methanol synthesis component within the spent CZA-ZSM-5@500 specimen by STEM-HAADF analysis. The size of Cu-based nanoparticles is comprised between 6 and 26 nm when located on the ZSM-5 grains, but the particles remain preferentially located on the ZnO and alumina grains.

Figure 12. Rate of deactivation of CZA-ZSM-5 catalysts as a function of the concentration of Brönsted acid sites on the zeolite external surface measured by lutidine adsorption.

Figure S1. Histograms of zeolite particle size distribution measured from SEM images.

Figure S2. XRD patterns of CZA catalyst.

Figure S3. TEM image of activated CZA catalyst

Figure S4. TPR profile of CZA catalyst

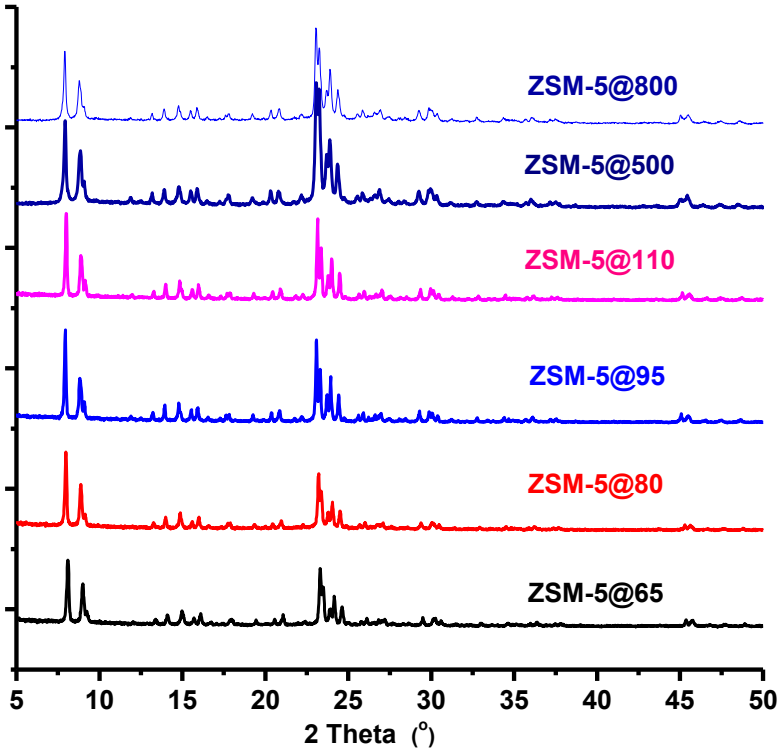

1

2

3 **Figure 1.** XRD patterns of ZSM-5 samples. The patterns are offset for clarity

4

5

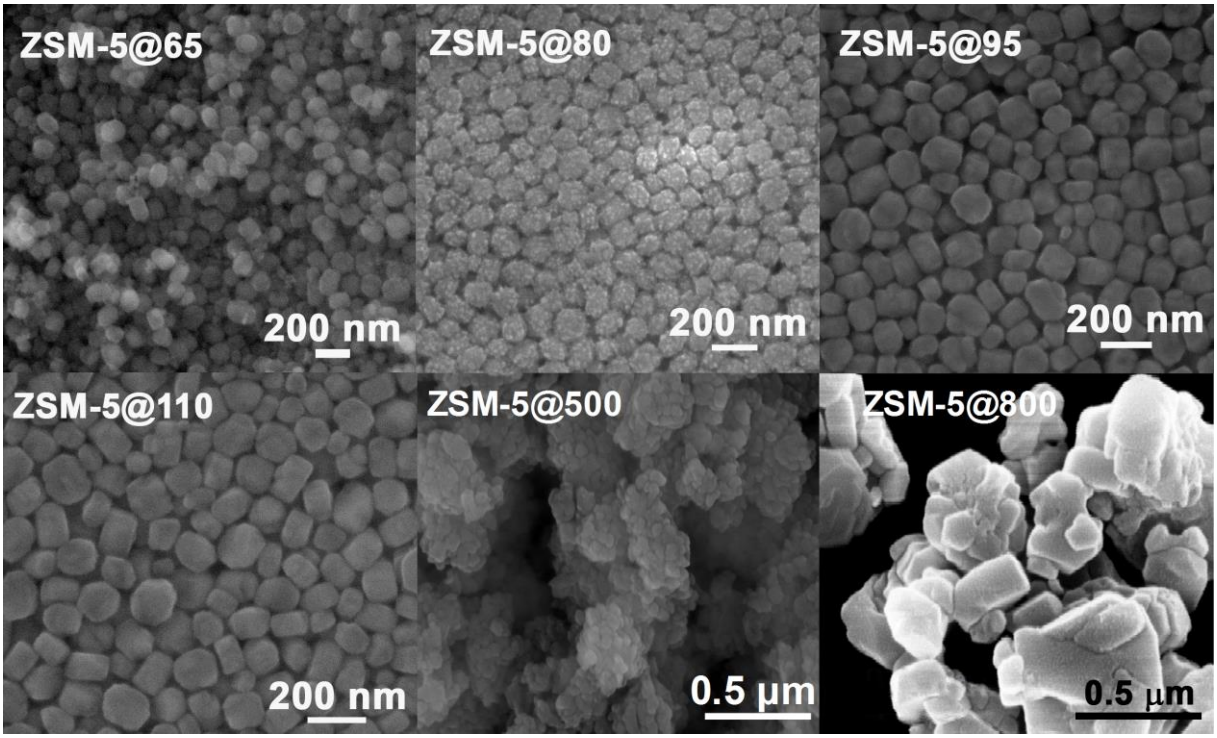

Figure 2. Representative SEM images of the series of ZSM-5 samples.

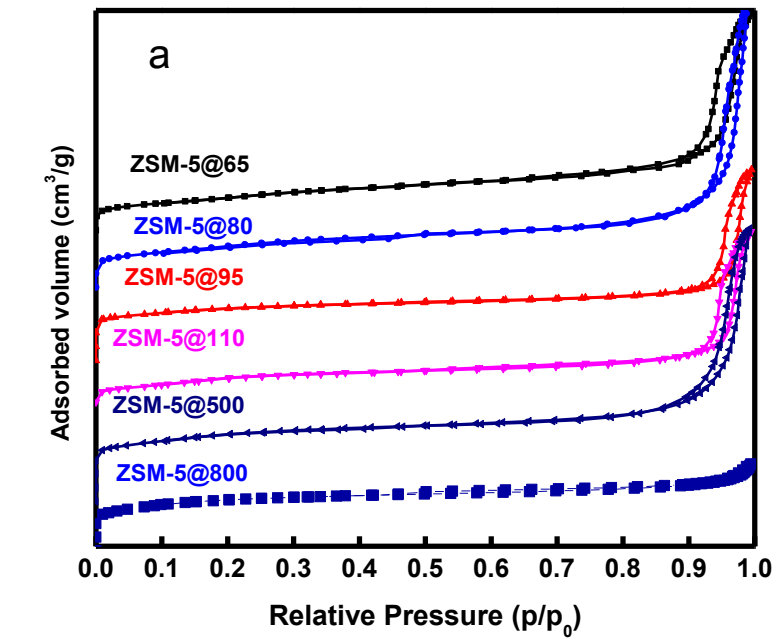

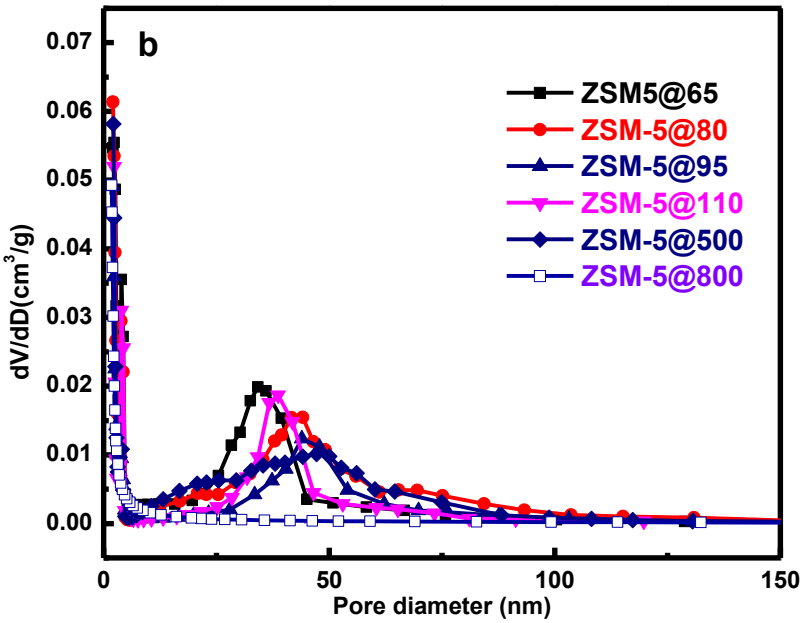

Figure 3. Nitrogen adsorption-desorption isotherms (a) and BJH mesopore size distribution curves. The nitrogen adsorption-desorption isotherms are offset for clarity.

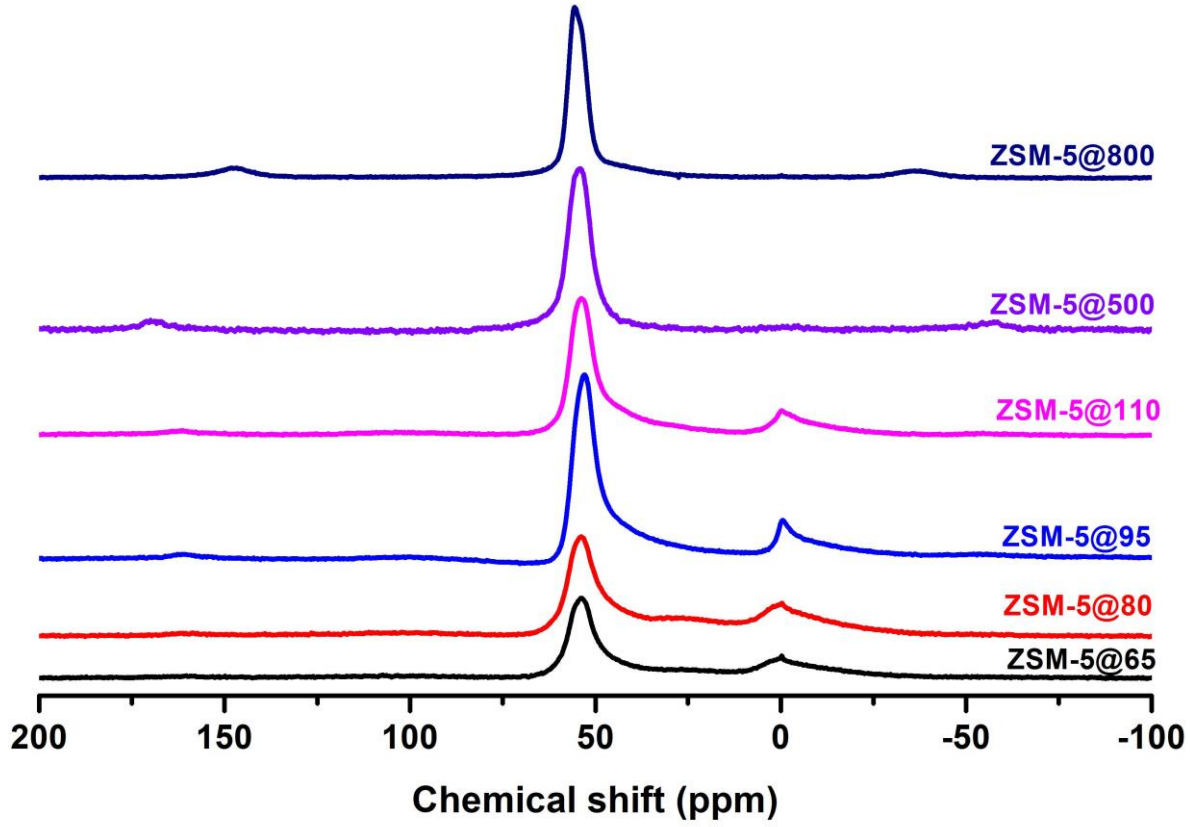

Figure 4. Normalized ^{27}Al MAS NMR spectra of the series of ZSM-5 samples. The spectra are offset for clarity.

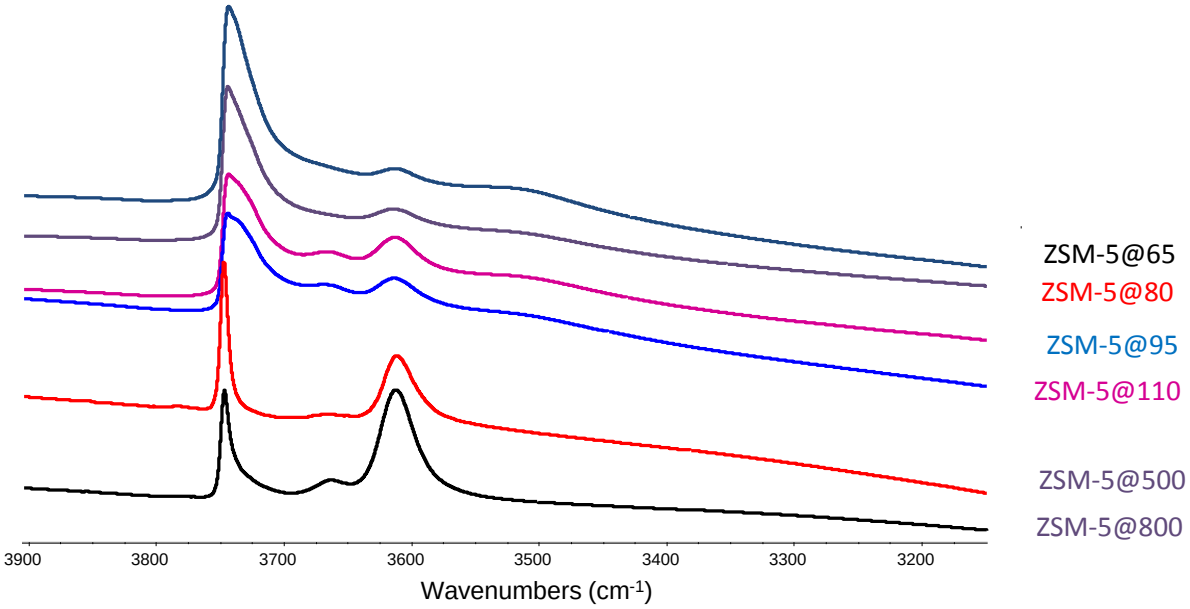

Figure 5. FTIR spectra of zeolites in the region of OH stretching vibrations. The spectra are offset for clarity.

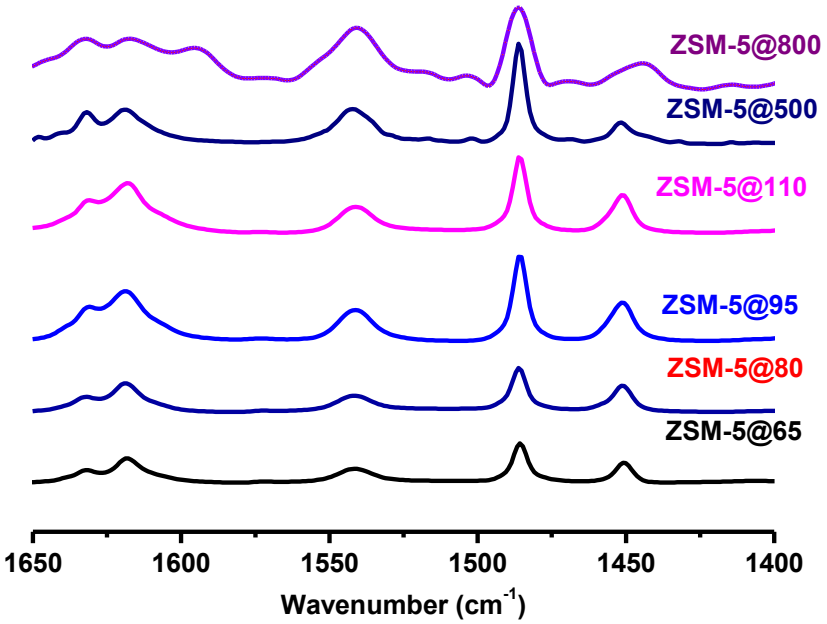

Figure 6. FTIR spectra of zeolites with adsorbed pyridine. The spectra are offset for clarity.

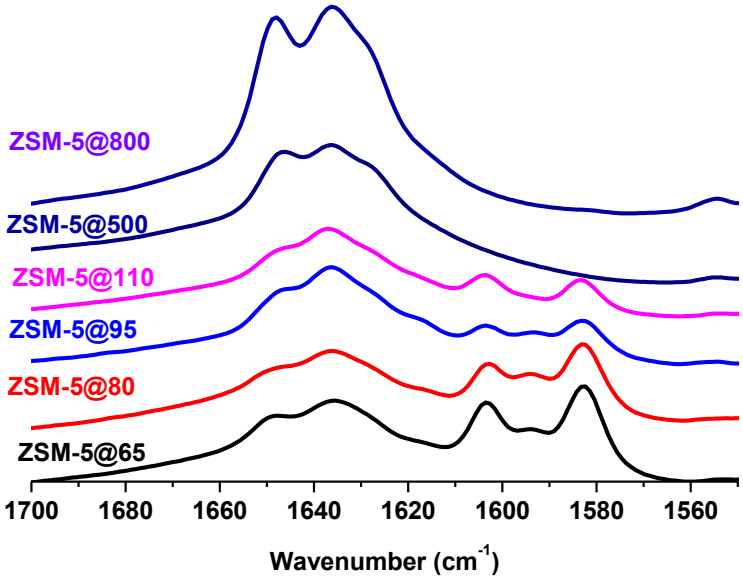

Figure 7. FTIR spectra of zeolites with adsorbed lutidine. The spectra are offset for clarity.

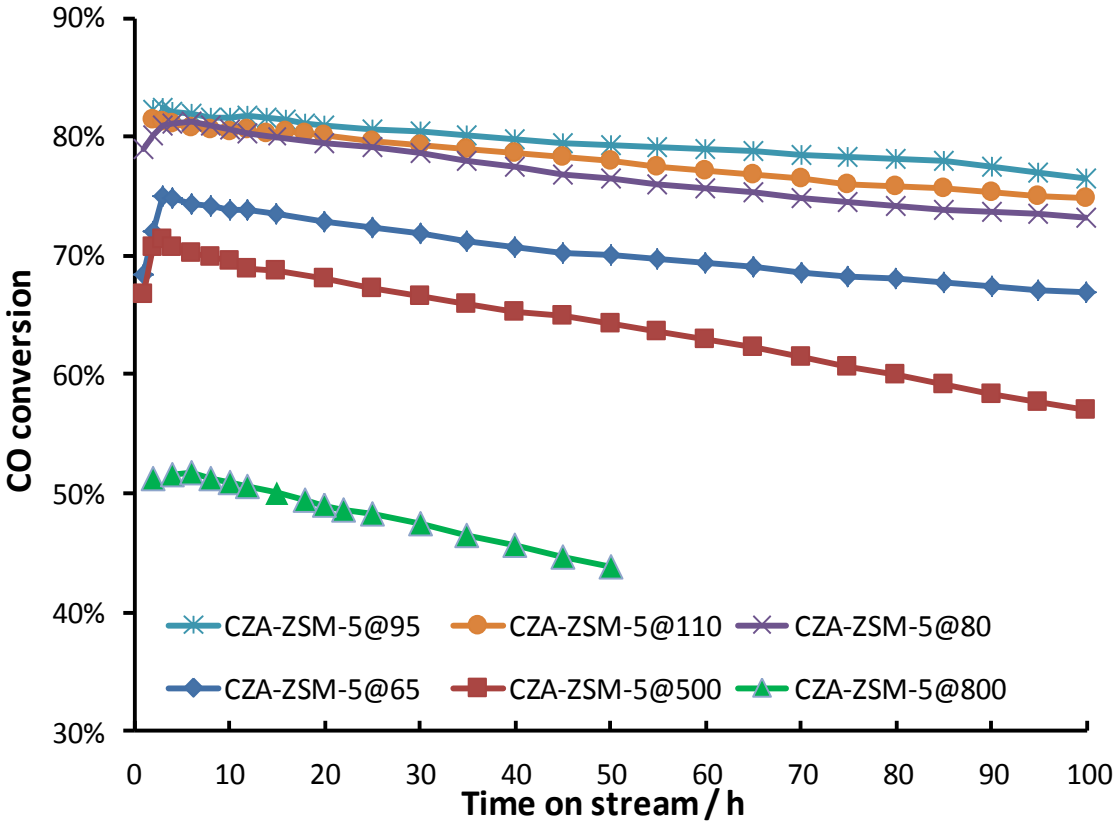

Figure 8. Carbon monoxide conversion on the hybrid CZA-ZSM-5 catalysts as function of time on stream (T=260 °C, P=20 bar, $H_2/CO=2$, GHSV=3600 cm^3/g_{cat} h)

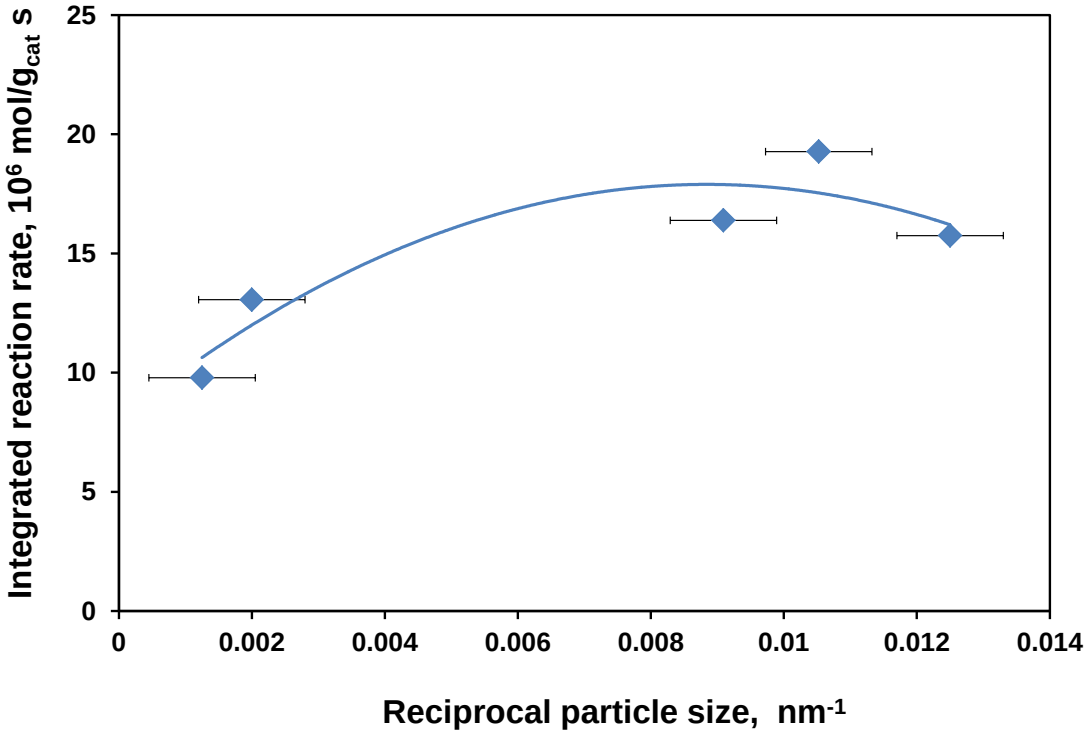

Figure 9. Reaction rate as a function of reciprocal zeolite particle size in hybrid CZA-ZSM-5 catalysts (T=260 °C, GHSV=7200 cm^3/g_{cat} h, P=20 bar, $H_2/CO=2$).

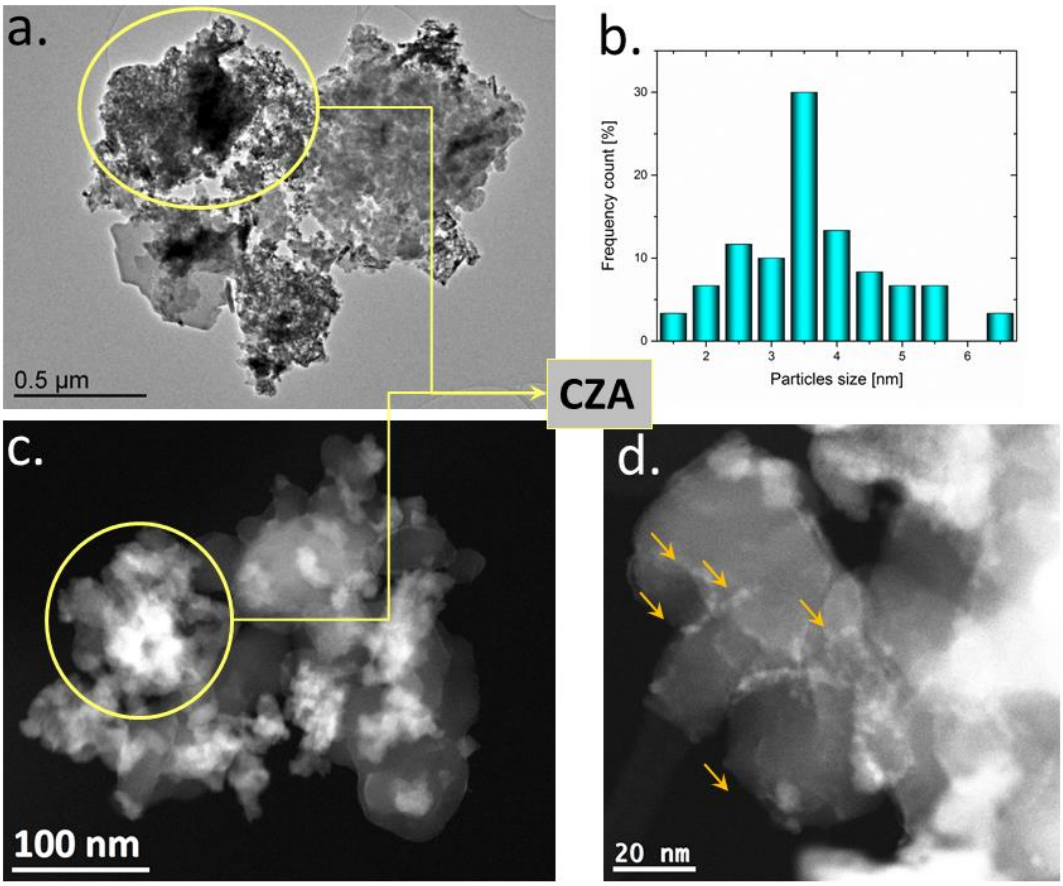

Figure 10. Localization of copper methanol synthesis component within the fresh CZA-ZSM-5@500 containing larger intergrown zeolite agglomerates by STEM-HAADF analysis. Cu-based nanoparticles with sizes between 2 and 7 nm are disposed on the ZSM-5 grains or on the surface of the ZnO and alumina grains.

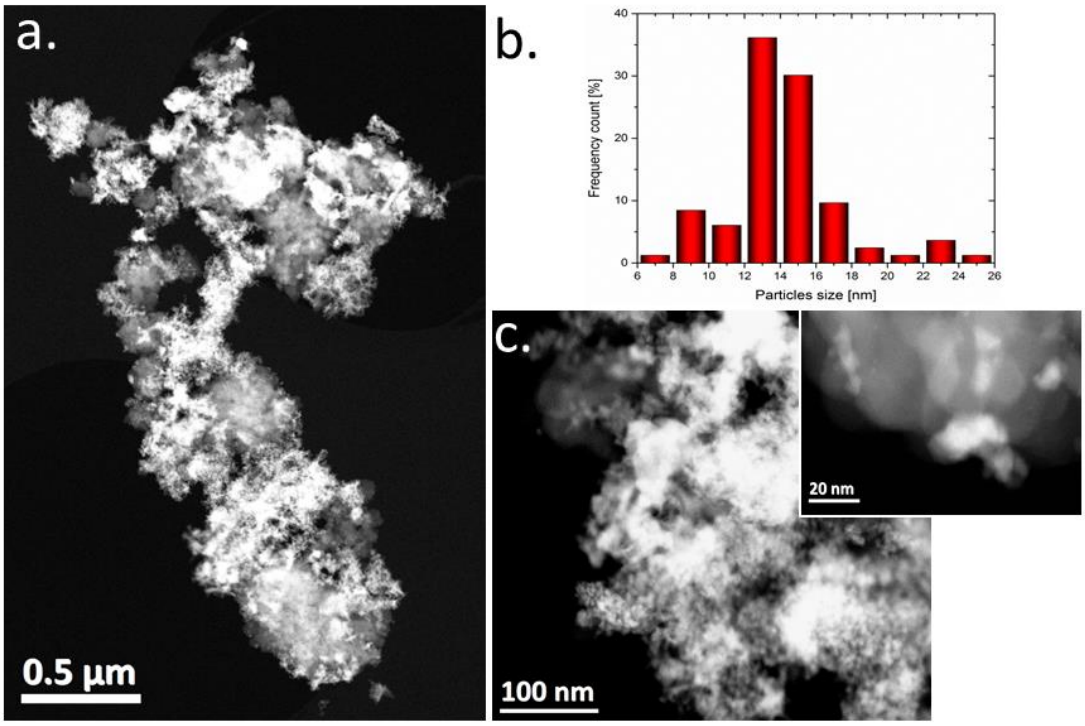

Figure 11. Localization of copper methanol synthesis component within the spent CZA-ZSM-5@500 specimen by STEM-HAADF analysis. The size of Cu-based nanoparticles is comprised between 6 and 26 nm when located on the ZSM-5 grains, but the particles remain preferentially located on the ZnO and alumina grains.

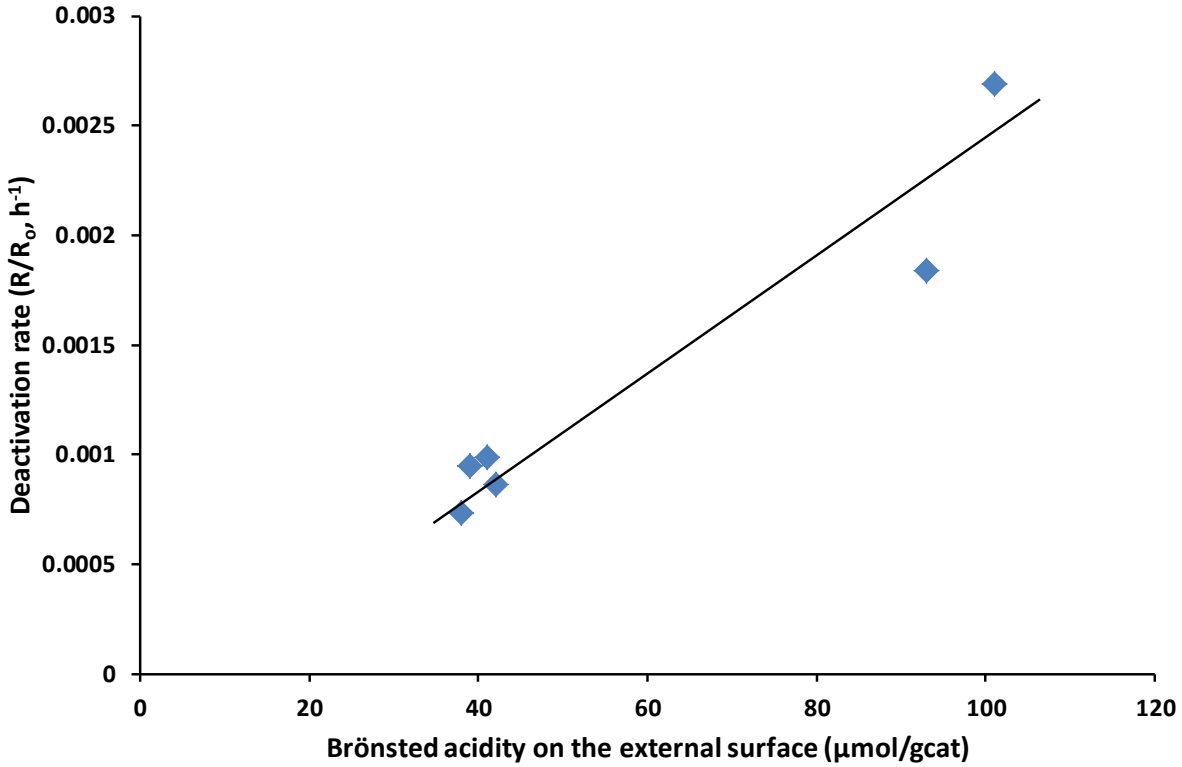

Figure 12. Rate of deactivation of CZA-ZSM-5 catalysts as a function of the concentration of Brönsted acid sites on the zeolite external surface measured by lutidine adsorption.

Table 1.

Characterization of ZSM-5 zeolites

Zeolite	Si/Al ratio from ICP	*Part. size, nm	S_{BET} m^2/g	S_{ext} m^2/g	S_{micro} m^2/g	V_{total} cm^3/g	V_{micro} cm^3/g	Py ads, μmol/gcat		Lu ads. BS* $\mu mol/g_{cat}$
								BS**	LS**	
ZSM-5@65	36	63	382	206	176	0.586	0.093	72	53	39
ZSM-5@80	24	83	395	201	194	0.627	0.104	83	69	41
ZSM-5@95	31	100	352	182	170	0.544	0.095	183	122	38
ZSM-5@110	27	110	369	180	189	0.493	0.092	143	282	42
ZSM-5@500	45	456	383	197	186	0.529	0.091	160	60	93
ZSM-5@800	25	810	381	139	242	0.258	0.118	367	119	101

*Sauter (3,2) average particle size calculated from histograms shown in Figure S1 (SM).

**BS is Brönsted acid sites, LS is Lewis acid sites.

Table 2.

Catalytic performance of the hybrid CZA-ZSM-5 catalysts in direct DME synthesis (T=260 °C, P=20 bar) at different GHSV.

Catalyst	Integral reaction rate, 10^{-6} $mol_{CO}/s\ g_{cat}$	Conversion, %	S_{CH3OH}, %	S_{DME}, %	S_{CO2}, %	S_{HC}, %
GHSV=3600 cm^3/g_{cat} h						
CZA/ZSM-5@65	9.82	75.0	4.5	69.8	25.3	0.40
CZA/ZSM-5@80	10.6	81.1	1.6	72.3	25.9	0.20
CZA/ZSM-5@95	10.7	82.2	1.6	71.4	26.6	0.40
CZA/ZSM-5@110	10.7	81.4	0.9	72.5	26.3	0.30
CZA/ZSM-5@500	9.3	71.3	5.4	67.7	27.3	0.10
CZA/ZSM-5@800	6.7	51.2	22.3	56.7	19.1	1.9
GHSV=7200 cm^3/g_{cat} h						
CZA/ZSM-5@80	15.8	56.8	0.9	73.3	25.5	0.3
CZA/ZSM-5@95	19.3	69.5	1.1	73.4	25.1	0.4
CZA/ZSM-5@110	16.4	59.1	0.8	73.4	25.5	0.3
CZA/ZSM-5@500	13.1	47.1	6.1	68.6	25.1	0.2
CZA/ZSM-5@800	9.8	35.3	18.2	48.7	32.2	1.0
GHSV=14400 cm^3/g_{cat} h						
CZA/ZSM-5@80	18.9	34	1.5	73.0	25.3	0.20
CZA/ZSM-5@95	26.0	46.8	1.0	73.9	24.8	0.30
CZA/ZSM-5@110	20.5	37	1.1	73.2	25.3	0.40
CZA/ZSM-5@500	14.4	26	1.5	71.3	27	0.20

Table S1. Fractions[a] of tetra-(f(Al^{IV})), penta-(f(Al^{V})) and hexa-(f(Al^{VI})) coordinated aluminum species in nanosized sample calculated from deconvoluted[b] ^{27}Al MAS NMR and the amounts of Lewis acid sites determined from the IR experiments.

Reference

1 G. A. Olah, A. Goeppert, G.K.S. Prakash, J. Org. Chem. 74 (2008) 487−498.

2 J. Sun, G. Yang, Y. Yoneyama, N. Tsubaki, ACS Catalysis 4 (2014) 3346-3356.

3 R. Anggarani, C.S. Wibowo, D. Rulianto, Energy Procedia 47 (2014) 227-234.

4 T. Ogawa, N. Inoue, T. Shikada, Y. Ohno, J. Nat. Gas Chem. 12 (2003) 219-227

5 G.R. Moradi, J. Ahmadpour, F. Yaripour, J. Wang, Can. J. Chem. Eng. 89 (2011) 108-115.

6 H.-J. Chen, C.-W. Fan, C.-S. Yu, Appl. Energy 101 (2013) 449-456

7 G. R. Moradi, J. Ahmadpour, F. Yaripour, J. Wang, Can. J. Chem. Eng. 89 (2011) 108-115.

8 K. Fujimoto, K. Asami, T. Shikada, H. Tominaga, Chem. Lett. 13 (1984) 2051-2054.

9 W.J. Shen, K.W. Jun, H.S. Choi, K.W. Lee Korean J. Chem. Eng. 17 (2000) 210–216.

10 J. W. Jeong, C.-I. Ahn, D. H. Lee, S. H. Um, J. W. Bae, Catal. Lett. 143 (2013) 666–672.

11 J. W. Jung, Y. J. Lee, S. Ho Um, P. J. Yoo, D. H. Lee, K.-W. Jun, J. W. Bae, Appl. Catal. B 126 (2012) 1-8.

12 G. Yang, N. Tsubaki, J. Shamoto, Y. Yoneyama, Y. Zhang, J. Am. Chem. Soc. 132 (2010) 8129-8136.

13 R. Phienluphona, K. Pinkaewa, G. Yang, J. Li, Q. Wei, Y. Yoneyama, T. Vitidsant, N. Tsubaki, Chem. Eng. J. 270 (2015) 605-611.

14 G. Yang, M. Thongkam, T. Vitidsant, Y. Yoneyama, Y. Tan, N. Tsubaki, Catal. Today 171 (2011) 229-235.

15 G.C. Chinchen, K.C. Waugh, D. A.Whan. Appl Catal 25 (1986) 101-107.

16 M. Günter, T. Ressler, B. Bems, C. Büscher, T. Genger, O. Hinrichsen, M. Muhler and R. Schlögl. Catal. Lett. 71 (2001) 37-44.

17 J. Wagner, P. Hansen, A. Molenbroek, H. Topsøe, B. Clausen, S. Helveg. J. Phys. Chem. B 107 (2003) 7753-7758.

18 P. Hansen, J. Wagner, S. Helveg, J. Rostrup-Nielsen, B. Clausen, H. Topsøe. Science, 295 (2002) 2053-2055.

19 Y. Okamoto, K. Fukino, T. Imanaka, S. Teranishi, J. Phys. Chem. 87 (1983) 3747-3754.

20 S. Mehta, G.W. Simmons, K. Klier, R.G. Herman, J. Catal. 57 (1979) 339-360.

21 J.L. Li, X.G. Zhang, T. Inui, Appl. Catal. A 147 (1996) 23–33.

22 T. Takeguchi, K. Yanagisawa, T. Inui, M. Inoue, Appl. Catal. A 192 (2000) 201–209.

23 D. Mao, W. Yang, J. Xia, B. Zhang, G. Lu, J. Mol. Catal. A 250 (2006) 138–144.

24 I. Sierra, J. Ereñna, A.T. Aguayo, J.M. Arandes, J. Bilbao, Appl. Catal. B 94 (2010) 108–116.

25 V. Vishwanathan, K.-W. Jun, J. W. Kim, H. S. Roh, Appl. Catal. A 276 (2004) 251-255.

26 J. Fei, Z. Hou, B. Zhu, H. Lou, X. Zheng, Appl. Catal. A. 304 (2006) 49-54.

27 J.-H. Kim, M. J. Park, S. J. Kim , O.-S. Joo, K.-D. Jung, Appl. Catal. A 264 (2004) 37–41.

28 J. W. Bae, S.-H. Kang, Y.-J. Lee, K.-W. Jun, Appl. Catal. B 90 (2009) 426–435.

29 A. Ciftci, N.A. Sezgi, T. Dogu, Ind. Eng. Chem. Res. 49 (2010) 6753-6762.

30 K. S. Yoo, J.-H. Kim, M.-J. Park, S.-J. Kim, O.-S. Joo, K.-D. Jung, Appl. Catal. A 330 (2007) 57–62.

31 F. Yaripour, F. Baghaei, I. Schmidt, J. Perregaard, Catal. Commun. 6 (2005) 542-549.

32 A. García-Trenco, S. Valencia, A. Martínez, Appl. Catal. A 468 (2013) 102– 111.

33 M. Stiefel, R.Ahmad, U. Arnold, M. Döring, Fuel Process. Technol. 92 (2011) 1466−1474.

34 H. Zhang, W. Li, W. Xiao, Intern. J. Chem. React. Engineering 10 (2012) A82

35 F. S. R. Barbosa, V. S. O. Ruiz, J. L. F. Monteiro, R. R. de Avillez, L. E. P. Borges, L. G. Appel, Catal. Lett. 126 (2008) 173-178.

36 R. Montesano, A. Narvaez, D. Chadwick, Appl. Catal. A 482 (2014) 69-77.

37 A. Ciftci, D. Varisli, K. Cem Tokay, N. Asli Sezgi, T. Dogu, Chem. Eng. J. 207-208 (2012) 85-93.

38 A. García-Trenco, A. Martínez, Appl. Catal. A 493 (2015) 40–49.

39 I. Sierra, J. Ereña, A.T. Aguayo, J.M. Arandes, M. Olazar, J. Bilbao, Appl. Catal. B 106 (2011) 167-173.

40 V.V. Ordomsky, M. Cai, V. Sushkevich, S. Moldovan, O. Ersen, C. Lancelot, V. Valtchev, A.Y. Khodakov, Appl. Catal. A 486 (2014) 266–275.

41 P.B. Weisz, V.J. Frilette, J. Phys. Chem. 64 (1960) 382-382.

42 T.F. Degnan, J. Catal. 216 (2003) 32–46.

43 B. Smit, T. L. M. Maesen, Nature 451 (2008) 671-678.

44 E. J.C. Verheyen, M. Kurttepeli, G. Vanbutsele, E. Gobechiya, T.I. Korányi, S. Bals, G. Van Tendeloo, R. Ryoo, C.E.A. Kirschhock, J.A. Martens, J. Catal. 300 (2013) 70-80.

45 B.D. Vandegehuchte, J.W. Thybaut, A. Martínez, M.A. Arribas, G.B. Marin, Appl. Catal. A 441-442 (2012) 10-20.

46 R. E. Jentoft, M. Tsapatsis,y M. E. Davis, B. C. Gates, J. Catal. 179 (1998) 565–580.

47 L. Bonetto, M.A. Camblor, A. Corma, J. Perez-Pariente, Appl. Catal. A 82 (1992) 37-50.

48 Y. J. Lee, J.-H. Kim, S. H. Kim, S. B. Hong, G. Seo, Appl. Catal. B 83 (2008) 160–167.

49 J. H. Lee, M. B. Park, J. K. Lee, H.-K Min, M. K. Song, S. B. Hong, J. Am. Chem. Soc. 132 (2010) 12971–12982.

50 H.-G. Jang, H.-K Min, J. K. Lee, S. B. Hong, G. Seo, Appl. Catal. A 437– 438 (2012) 120–130.

51 E.P. Barrett, L.G. Joyner,, P.P. Halenda, J. Am. Chem. Soc. 73 (1951) 373-380.

52 J.H. de Boer, B.C. Lippens, B.G. Linsen, J.C.P. Broekhoff, A. van den Heuvel, Th.V. Osinga, J. Colloid Interface Sci. 21 (1966) 405-414.

53 C.A. Emeis, J. Catal. 141 (1993) 347-354.

54 T. Onfroy, G. Clet, M. Houalla, Micropor. Mesopor. Mater. 82 (2005) 99-104.

55 M. Firoozi, M. Baghalha, M. Asadi, Catal. Commun. 10 (2009) 1582-1585.

56 J.H. De Boer, "The Structure and Properties of Porous Materials". D. H. Everett and F.S. Stone (eds). London, Butterworths, 68-94 (1958).

57 G. Majano, A. Darwiche, S. Mintova, V. Valtchev, Ind. Eng. Chem. Res. 48 (2009) 7084-7091.

58 J.A. Lercher, A. Jentys, Stud. Surf. Sci. Catal. 168 (2007) 435-476.

59 A. Zecchina, S. Bordiga, G. Spoto, D. Scarano, G. Petrini, G. Leofanti, M. Padovan, C. Otero Aeran, J. Chem. Soc., Faraday Trans. 88 (1992) 2959-2969.

60 K. Barbera , F. Bonino , S. Bordiga , T.V.W. Janssen, P. Beato , J. Catal. 280 (2011) 196-205.

61 Z. Qin, L. Lakiss, L. Tosheva, J.-P. Gilson, A. Vicente, C. Fernandez, V. Valtchev, Adv. Funct. Mater. 24 (2014) 257-264

62 Kiricsi, C. Flego, G. Pazzuconi, W. O. Jr. Parker, R. Millini, C. Perego, G. Bellussi, J. Phys. Chem. 98 (1994) 4627–4634.

63 G. Crépeau, V. Montouillout, A. Vimont, L. Mariey, T. Cseri, F. Mauge, , J. Phys. Chem. B 110 (2006) 15172-15185.

64 F. Thibault-Starzyk, I. Stan, S. Abelló, A. Bonilla, K. Thomas, C. Fernandez, J.-P. Gilson, J. Pérez-Ramírez, J. Catal. 264 (2009) 11–14

65 J.M. Beiramar, A. Griboval-Constant, A. Y. Khodakov, ChemCatChem 6 (2014) 1788-1793.

66 C. Baltes, S Vukojevic, F. Schuth, J. Catal. 258 (2008) 334-344.

67 J. L. Li, T. Inui, Appl. Catal. A 137 (1996) 105-117.

68 M. Migliori, A. Aloise, G. Giordano, Catalysis Today 227 (2014) 138–143.

69 P.B. Weisz, Adv. Catal. 13 (1962) 137-190.

70 J. Čejka, H. van Bekkum, A. Corma, F. Schüth, Introduction to Zeolite Science and Practice (third ed.) Elsevier Science (2007).

71 M. Choi, K. Na, J. Kim, Y. Sakamoto, O. Terasaki, R. Ryoo, Nature 461 (2009) 246-249.

72 N. Batalha, L. Pinard , C. Bouchy, E. Guillon, M. Guisnet, J. Catal. 307 (2013) 122–131.

73 J. Kim, W. Kim, Y. Seo, J.-C. Kim, R. Ryoo, J. Catal. 301 (2013) 187–197.

74 A. García-Trenco, A. Martínez, Catal. Today 227 (2014) 144–153.